

In situ x-ray and neutron diffraction investigation of Bi-2212 in multifilamentary wires during thermal treatment

Alberto Martinelli,¹ Emilio Bellingeri,¹ Alessandro Leveratto,¹ Luca Leoncino,¹ Clemens Ritter,² and Andrea Malagoli^{1,*}

¹CNR-SPIN, Corso Perrone 24, 16152, Genova, Italy

²Institut Laue-Langevin, 71 Avenue des Martyrs, 38042 Grenoble, Cedex 9, France



(Received 2 May 2018; revised manuscript received 21 June 2018; published 3 August 2018)

Significant insights for critical current density (J_c) improvement in Bi-2212 superconductor wires can be obtained by an accurate analysis of the structural and microstructural properties evolving during the so-called partial-melt process, a heat treatment needed to improve grain connectivity and therefore gain high J_c . Here, we report an *in situ* analysis by means of synchrotron x-ray and neutron diffraction performed, for the first time, during the heat treatment carried out with the very same temperature profile and reacting oxygen atmosphere in which the Bi-2212 wires are usually treated for practical applications. The obtained results show the thermal evolution of the Bi-2212 structure, focusing in particular on texturing and secondary phases formation. The role of the oxygen is discussed as well. Hence, the present investigation marks a significant advance for the comprehension of the phenomena involved in the wire fabrication process and provides useful insights for the process optimization as well.

DOI: [10.1103/PhysRevMaterials.2.084801](https://doi.org/10.1103/PhysRevMaterials.2.084801)

I. INTRODUCTION

Scientific applications involving magnet construction for the energy upgrade of Large Hadron Collider (LHC), for fusion (ITER) or for nuclear magnetic resonance magnets require superconducting materials capable of generating magnetic fields above 20 T, once wound as magnets [1,2]. High temperature superconductors such as $\text{YBa}_2\text{Cu}_3\text{O}_{7-x}$ (YBCO), $(\text{BiPb})_2\text{Sr}_2\text{Ca}_2\text{Cu}_3\text{O}_{10-x}$ (Bi-2223), and $\text{Bi}_2\text{Sr}_2\text{CaCu}_2\text{O}_{8+x}$ (Bi-2212) show flat J_c behavior up to fields above 30 T due to H_{c2} exceeding 100 T [3]. Among these, Bi-2212 wires exploit a very flexible technology: they can be processed as round conductor with fine and twisted filaments arranged in multiple architectures. The metallic sheath has a high thermal conductivity and there is no need for any diffusion barrier. However, the significantly low critical current density (J_c) of Bi-2212 wires has been the bottleneck for a long time to their application for magnet construction. For several years, research works aimed to improve such transport properties were focused on the analysis of the Bi-2212 phase formation trying to reveal the relationship between processing, microstructure, and superconducting properties. Despite that, recent reports [4–7] revealed that the internal gas pressure generated during the heat treatment produces the formation of bubbles inside the wire and the density of the superconducting filaments is reduced. Such a phenomenon has been recognized as the main hindrance for J_c enhancement in Bi-2212 wires. The application of a gaseous Over Pressure (OP; 50–100 bar) during the heat treatment has been proposed to increase the density of the Bi-2212 filaments and thus J_c [8]. The samples obtained by the OP process show engineering critical current density (J_c) values of 800–900 A/mm² at high fields, well above

the application requirements ($J_c = 400\text{--}600$ A/mm²). As an alternative route to the OP process, an innovative mechanical deformation has been proposed by our group [9–11] with the aim to realize dense wires with superconducting properties that could satisfy the application requirements through a more attractive process for an industrial scaling-up. In such a context, significant insights for J_c improvement in this material can still be obtained by an accurate analysis of the evolution of the structural and microstructural properties during the so-called partial-melt process (PMP), a heat treatment needed to improve grain connectivity and therefore gain high J_c . Such a process involves the heating of Bi-2212 powders contained into the Ag sheath above the peritectic temperature ($\sim 882^\circ\text{C}$); as a result, Bi-2212 decomposes into a melt plus solid $(\text{SrCa})_{14}\text{Cu}_{24}\text{O}_{4x}$ (14:24 AEC) and $\text{Bi}_2(\text{SrCa})_4\text{O}_x$ (2:4 CF) phases. During subsequent slow cooling this mixture reacts, forming well-connected Bi-2212 phase. The final annealing and subsequent cooling at room temperature lead to an oxygen overdoping, enhancing the transport properties at high fields [12]. The investigation of the phase assemblage in Ag-sheathed Bi-2212 wires and its evolution during thermal treatment has been the subject of several studies. Zhang and Hellstrom [13] found that the phase assemblage forming after the incongruent melting of Bi-2212 is strongly dependent on the O_2 partial pressure in the reacting atmosphere. Recent works showed an extensive formation of Bi-2201 ($\text{Bi}_2\text{Sr}_2\text{CuO}_6$) intergrowths within Bi-2212 grains [14]. The presence of Bi-2201 and secondary phases in fully reacted wires can represent a limit in reaching very high J_c even in very dense filaments. All of these studies were performed using SEM-EDX analysis on fully reacted wires and/or samples quenched from high temperature to room temperature. A first attempt to an *in situ* analysis was performed by C. Scheuerlein *et al.* [15] but here, the phases and structure evolution have been analyzed during the complete heat treatment, where each step has been accurately monitored

*andrea.malagoli@spin.cnr.it

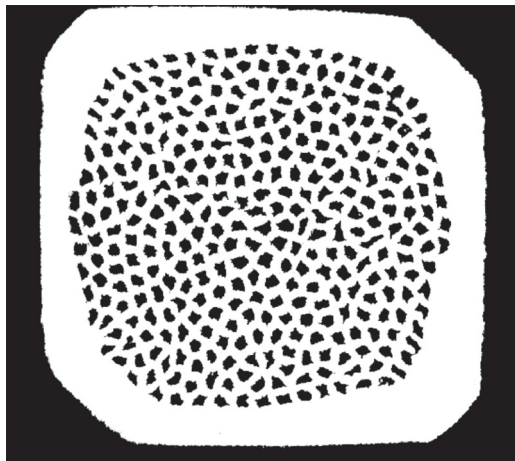


FIG. 1. Cross-section of the multifilamentary wire: $0.7 \times 0.7 \text{ mm}^2$ in size and 331 filaments.

in terms of heating/cooling rate, temperature, and duration. Actually, neither the processes occurring during each step of the heat treatment nor the role of the oxygen pressure are yet completely understood. We recently applied, for the first time to the Bi-2212 superconductor, a model based on the proximity effect to describe the nature of the grain boundaries through the behavior of J_c as a function of the temperature in samples with different oxygen content in the overdoping regime [16].

In the present work, we report the results of an *in situ* investigation of Bi-2212 wires, carried out throughout the thermal treatment performed in the very same conditions usually applied in the production process. In particular, the reported results illustrate how the Bi-2212 and the secondary intergrowth phase Bi-2201 evolve during the thermal treatment as well as the major role played by the oxygen activity in the reacting atmosphere for crystallization and texturing. The reported results are hence important not only for the comprehension of the phenomena involved during the wire fabrication process, but also because they can provide useful insights for the optimization of the process itself.

II. EXPERIMENTAL

The investigated samples were prepared using the powder-in-tube method (PIT), starting by filling an Ag tube with outer (OD) and inner (ID) diameters of 15 and 11 mm, respectively, with Nexans granulate powder of composition $\text{Bi}_{2.16}\text{Sr}_{1.93}\text{Ca}_{0.89}\text{Cu}_{2.02}\text{O}_x$. After drawing, the obtained monofilamentary wire is hexagonally shaped, cut in 331 pieces, and restacked in a 18/15 mm (OD/ID) Ag/Mg alloy tube. It is then cold worked with a proper alternation of drawing and groove-rolling steps. Finally, a square wire is obtained, having a $0.7 \times 0.7 \text{ mm}^2$ cross-section, an average size of the single filament of about 20–25 μm and a superconducting fill factor of about 22%. In the above described process, the new concept for the densification of powders before the PMP is used [9], namely a proper alternation of drawing and groove-rolling steps that drastically reduces the porosity and leads to a powder density inside the filaments much higher than that obtained by the

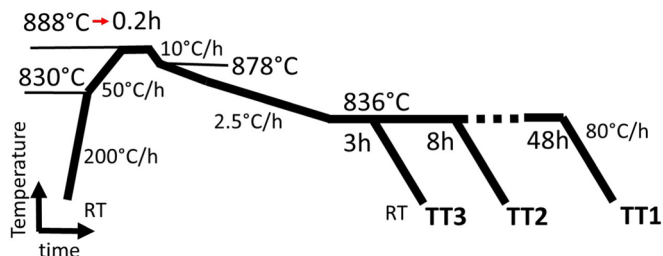


FIG. 2. Scheme (not in scale) of the thermal treatment profiles (temperature versus time) used during experiments. The three treatments have the same temperature profile from the beginning until the plateau at 836°C, whereas they differ in the duration of the plateau itself.

standard process with just a drawing deformation. Figure 1 shows the cross-section of a multifilamentary wire.

The heat treatment optimized by Oxford Superconducting Technology for their commercial Bi-2212 wires, commonly used for conductor and magnet development, has been selected as a reference during our experiments (Fig. 2; TT1). The sample wire, after being processed with such thermal treatment, showed a critical current density $J_c = 2300 \text{ A/mm}^2$ at a temperature of 4.2 K and an applied magnetic field of 5 T. In the same condition of temperature and magnetic field, the wire processed in air with the same thermal treatment TT1 showed a $J_c = 300 \text{ A/mm}^2$. Such values are in good agreement with the values reported in literature [16].

Due to the limitations dictated by the available beam time at the large scale facilities where the experiments were carried out, some changes were necessary, as hereafter described.

The *in situ* powder diffraction analyses throughout thermal treatments were carried out using x-ray radiation at the ID11 beamline of the European Synchrotron Radiation Facility (ESRF; Grenoble, France; wavelength $\lambda = 0.14082 \text{ \AA}$) and neutron radiation at the high-intensity D20 diffractometer ($\lambda = 2.4162 \text{ \AA}$) of the Institute Laue Langevin (ILL; Grenoble, France). In both experiments, the samples were placed in a furnace mounted directly on the neutron or x-ray beamline. Figures 3 and 4 illustrate the experimental set-up assembled at ESRF and ILL, respectively.

The x-ray diffraction (XRD) analysis at ID11 was carried out using a tubular furnace in an experimental set-up similar to the one used by Flukiger *et al.* [17]. The quartz tube was closed by two kapton plugs and suitably shaped radiation screens were realized; in this way, the incident and diffracted radiation can be transmitted without interference across a takeout angle of about 3° . Single multifilamentary wires were then reacted under both an O_2 flux and an air flux using the thermal treatments TT2 and TT3, respectively (Fig. 2). XRD patterns were collected in transmission geometry; a two-dimensional detector was used and images were integrated along the azimuthal direction to obtain q-scan type measurements for the study of the phase evolution.

To optimize the available beam-time, the thermal treatments were arranged as follows: the plateau step has been reduced at 3 h and 8 h instead of 48 h for the treatments in air (TT3) and O_2 (TT2), respectively. To obtain a more complete analysis, data collection at room temperature has been performed on

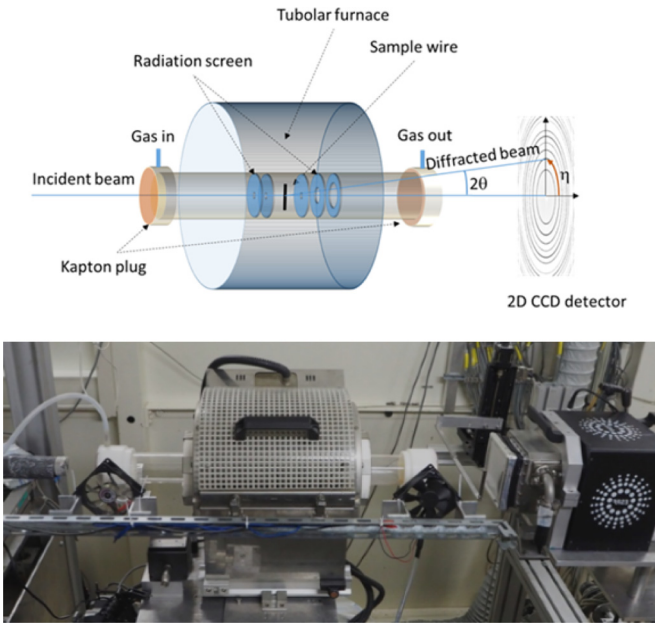


FIG. 3. Experimental set-up employed during XRD data collection at the ID11 beamline of ESRF. The 2θ Bragg angle and η azimuthal angle are indicated.

samples that previously underwent the whole heat treatment TT1 in our laboratories (fully reacted samples) in both air and O_2 atmosphere. At this scope, data collection was also carried out at room temperature without the heating furnace, thus providing diffraction patterns with wider angular ranges. To estimate the weight percentage of the coexisting Bi-2212 and Bi-2201 phases, these data were fitted using the Rietveld method.

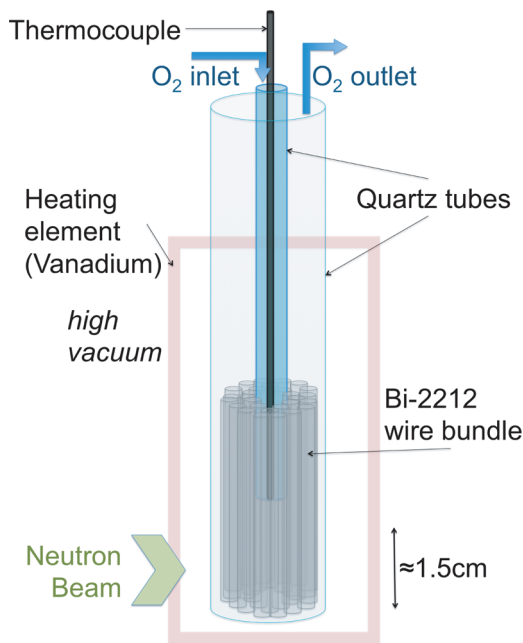


FIG. 4. Experimental set-up of the samples used in the neutron diffraction experiment at ILL.

The neutron powder diffraction (NPD) patterns were collected on a bundle of multifilamentary wires under an O_2 flux and using the thermal treatment TT2. In the neutron experiment, an ILL vanadium furnace was used; the sample was inserted inside a quartz tube and held at the optimal position by a second smaller quartz tube having the additional function of O_2 inlet. A Pt/PtRh thermocouple in contact with the wire bundle was used for the feedback control of the temperature [18].

The accuracies of both furnaces used during the XRD and NPD experiments are $\pm 0.5^\circ C$ on the length of the samples themselves.

Both NPD and XRD data were used to evaluate the phase evolution as well as the thermal dependence of microstructural properties of Bi-2212. Noteworthy: Most of the radiation scattered by the internal filaments is absorbed by the external Ag sheath. For this reason, structural refinements cannot be carried out; nonetheless, Le Bail fittings (profile matching) can be reliably performed. At this scope fitting was carried out using the program FULLPROF [19] using a file describing the instrumental resolution function and refining the scale factor, the zero point of detector, the background, the unit cell parameters, selected profile parameters, and the preferred orientation parameters. The microstructural properties of the Ag sheath were inspected by means of the Williamson-Hall method [20]; in particular, in the Williamson-Hall plots, a straight line passing through the origin and all the points of the different orders of the same reflection is obtained, whose slope provides a qualitative evaluation of the microstrain contribution. In addition, the texture was evaluated by analyzing the azimuthal distribution of the XRD peak intensity.

After the thermal treatment 1, Bi-2212 powders extracted from the wires were analyzed by x-ray powder diffraction analysis (XRPD; PANalytical X'Pert PRO; CuK_{α}). The crystal structures were refined according to the Rietveld method [21]; refinements were carried out using a file describing the instrumental resolution function. In the final cycle, the following parameters were refined: the scale factor, the zero point of detector, the background (parameters of the fifth-order polynomial function), the unit cell parameters, the atomic site coordinates not constrained by symmetry, the atomic displacement parameters, the anisotropic strain parameters, and the preferred orientation parameters.

III. RESULTS

A. Structural properties of Bi-2212

Despite its attractive physical and technological properties, a comprehensive investigation of the structural properties at high temperature of the Bi-2212 phase has not yet been carried out, to our knowledge. Structural studies performed at room temperature report both a tetragonal (space group $I4/mmm$) [22] as well as an orthorhombic (space group $Fmmm$) [23] symmetry. Rietveld refinement using x-ray powder diffraction data collected on the starting Bi-2212 powders suggests a tetragonal symmetry; in fact, no evident peak splitting of the tetragonal 110 diffraction line into the orthorhombic 200 and 020 ones can be appreciated. Figure 5 shows a representation

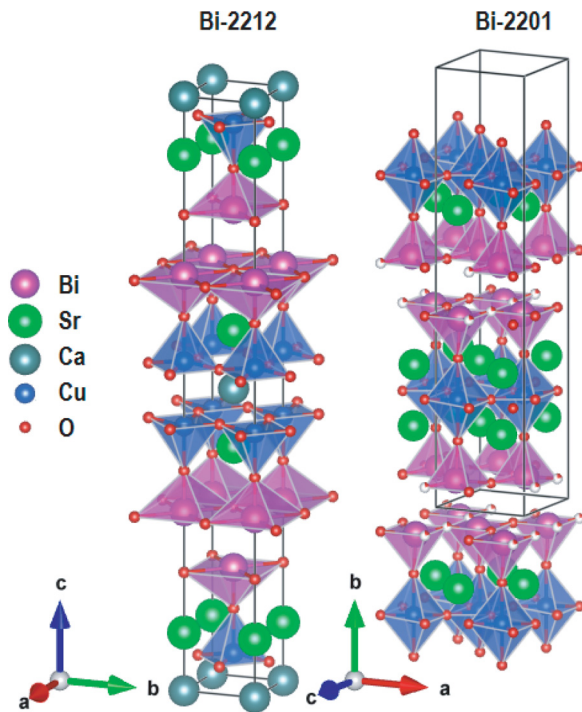


FIG. 5. Representation of the crystal structures of tetragonal Bi-2212 and Bi-2201.

of the layered structures of both $\text{Bi}_2\text{Sr}_2\text{Ca}_1\text{Cu}_2\text{O}_{8+x}$ (Bi-2212) and the closely related $\text{Bi}_2\text{Sr}_2\text{CuO}_6$ (Bi-2201) compound. Under suitable conditions, this structural correlation favours the intergrowth of Bi-2201 layers in melt-processed Bi-2212.

Figure 6 shows the comparison of the XRPD patterns for tetragonal Bi-2212 and Bi-2201 in the Q-range mainly inspected in the present work. For the sake of clarity, the position of these Bragg peaks serve as a reference, but can be affected by non-negligible shifts, depending on both the experimental

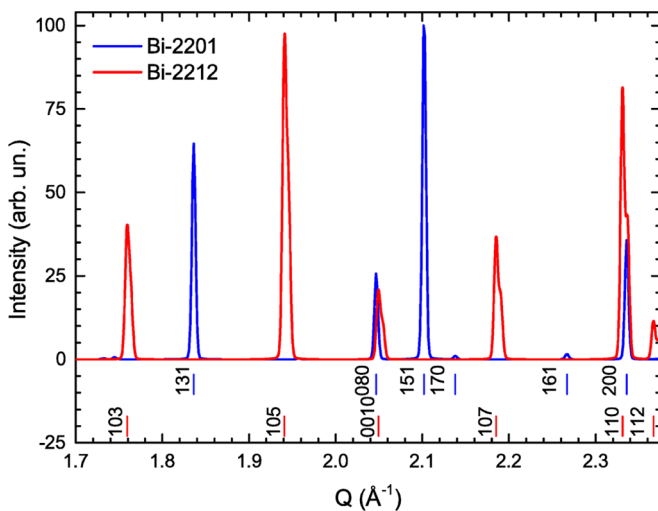


FIG. 6. Comparison of the calculated x-ray powder diffraction patterns for Bi-2212 and Bi-2201 (selected Q-range); vertical bars represent the position of the Bragg peaks (indexed).

set-up (zero shift of the diffractometer), temperature (thermal expansion), and chemical composition (mainly O content).

B. Structural refinement of Bi-2212 after thermal treatments

Table I lists the structural data of Bi-2212 extracted from the multifilamentary wires after the thermal treatments TT1 in air and O_2 (after Rietveld refinements using the laboratory XRPD data).

Rikel and Hellstrom [24] pointed out that the density of the Bi-2201 intragrowth layers (indicated with f) increases with the increase of the texturing degree; moreover, these authors reported a correlation between the intensity ratio of the 0 0 8 and 0 0 10 diffraction lines with the average $\langle f(1 - f) \rangle$ quantity. By applying this correlation, the density of the Bi-2201 layers intragrown within the Bi-2212 phase can be approximately estimated, being $\sim 6.5\%$ at maximum in the O_2 -treated sample and negligible in the air-treated sample. From these data, it can be concluded that the degree of texturing in our samples is significantly increased in the O_2 sample, a result that is confirmed by the *in situ* analysis data reported in Sec. III D.

C. Thermal evolution of the phase assemblage in the filaments

The thermal treatments at which the multifilamentary wires are submitted can be roughly divided into five main steps: (1) rapid heating up to 888°C , above the melting point of the Bi-2212 phase, (2) melting of the Bi-2212 phase, (3) texturing of the Bi-2212 phase on slow cooling, (4) plateau step at 836°C , and (5) cooling down to room temperature.

Figure 7 shows the XRD data from the multifilamentary wires collected during the melting step. In both samples, the Bi-2212 phase decomposes into the Bi-2201 phase (peaks at ~ 1.80 , ~ 2.07 and $\sim 2.32 \text{ \AA}^{-1}$) at $\sim 610^\circ\text{C}$ (~ 2.83 h). The observed intensities of the Bi-2201 Bragg peaks indicate that texturing is negligible at this stage, conversely to what was observed during the texturing step (*vide infra*). As the temperature further increases, the Bi-2201 phase decomposes, forming a novel Bi-2212 phase approximately at $\sim 850^\circ\text{C}$ (~ 4 h). Then, the Bi-2212 phase melts at the peritectic temperature ($\sim 882^\circ\text{C}$).

Upon melting, during the slow cooling step, some diffraction peaks can be detected in both air and O_2 treated filaments, but the correct identification of the corresponding phases is extremely challenging. Nonetheless, some clues can be gained: the occurrence of the $\text{Bi}_2(\text{SrCa})_4\text{O}_x$ (2:4 CF) phase can be mainly deduced from the presence of a main peak centered at $\sim 2.11 \text{ \AA}^{-1}$ (Fig. 7) and fainter ones at $\sim 1.21 \text{ \AA}^{-1}$ and $\sim 3.65 \text{ \AA}^{-1}$. Figure 8 shows the phase evolution as recorded by NPD in about the same Q-range as the x-ray data shown in Figure 7. It should be noted here that due to the different scattering lengths of the elements in x-ray and neutron diffraction, the intensities of the Bragg peaks can be very different. The peak at $\sim 2.11 \text{ \AA}^{-1}$ evidences the presence of the 2:4 CF phase again; unfortunately, the crystal structure of this phase at high temperature has not yet been resolved and hence it is challenging to discriminate its diffraction lines in a NPD pattern. Nonetheless, on account of their similar behavior, also the peaks at $\sim 2.20 \text{ \AA}^{-1}$, $\sim 2.27 \text{ \AA}^{-1}$, and $\sim 2.34 \text{ \AA}^{-1}$ can be

TABLE I. Structural parameters of Bi-2212 samples (laboratory XRPD data collected at 300 K after thermal treatments TT1; space group $I4/mmm$).

				Air			O ₂		
a (Å)				3.8202(1)			3.8242(1)		
c (Å)				30.8076(1)			30.7685(1)		
Atom	Wyckoff site	x	y	z	x	y	z		
Bi	4e	0	0	0.3019(1)	0	0	0.3012(1)		
Sr	4e	0	0	0.1094(1)	0	0	0.1109(1)		
Ca	2a	0	0	0	0	0	0		
Cu	4e	0	0	0.4485(1)	0	0	0.4509(1)		
O(1)	8g	0	1/2	0.0693(1)	0	1/2	0.0713(1)		
O(2)	4e	0	0	0.2215(1)	0	0	0.2304(1)		
O(3)	4e	0	0	0.3738(1)	0	0	0.3762(1)		
R _{Bragg} (%)				16.8			14.9		

presumptively ascribed to the 2:4 CF phase. In this context, it is worth noting that the Bi₆(Sr_{8-x}Ca_{3+x})O₂₂ ($-0.5 \leq x \leq 1.7$) compound reported by Luhrs *et al.* [25] likely corresponds to 2:4 CF phase, after comparison of the respective compositions and cell parameters.

Concerning the air treated sample, relatively strong diffraction lines are observed in the XRD patterns at 2.04, 2.07, and 2.10 Å⁻¹ during the melting step, consistent with previous investigations [15,26]. In these works, these peaks were ascribed to the presence of the high-temperature polymorph of the Bi₂(Sr_{4-x}Ca_x)O₇ phase. Actually, a closer inspection reveals their different trends over time (Fig. 9), suggesting that they are produced by distinct phases. The peak observed at 2.20 Å⁻¹ in the XRD patterns could be related to the (SrCa)₁₄Cu₂₄O₄₁ phase (14:24 AEC); its intensity decreases with time, whereas during the slow cooling faint peaks grow at ~0.95, 2.31, and 2.36 Å⁻¹; likely due to the formation of (SrCa)₂CuO₃ (2:1 AEC). This behavior is consistent with previous analyses carried out under an O₂ partial pressure ranging between 0.40 and 1.00 atm [13], where it was found that Bi-2212 melts incongruently forming the 2:4 CF and the 14:24 AEC phases, this last being replaced later by the 2:1 AEC phase.

D. Growth and texturing of the Bi-2212 phase from the melt

On further cooling, the Bi-2212 phase starts to grow, representing the main phase in both samples. The crystallization of the Bi-2212 phase from the melt is remarkably ruled by the reacting atmosphere. In the O₂-treated sample, the Bi-2212 phase starts to crystallize after ~6.58 h (876 °C), exhibiting an evident preferred orientation along [110] (Fig. 10). This result is consistent with previous studies carried out on round wires [27] and melt-cast processed polycrystalline tubes of Bi-2212 [28], where a preferred orientation along [100] or [010] was detected by assuming an orthorhombic structural model (in the orthorhombic structural model the a and b axes are rotated by 45° and these lattice parameters are a factor of √2 longer compared with the tetragonal a and b axes). Conversely, it starts to grow only after more than 9 h (869 °C) in the air-treated sample; also in this sample the preferred orientation along [110] is evident, but in this case the remaining diffraction peaks exhibit noticeable intensities, thus indicating a lower degree of texturing.

Figure 11 evidences the different time evolution of the integrated intensity for the tetragonal 110 peak of the Bi-2212 phase after its growth from the melt as obtained from the Le Bail fit for both O₂- and air-treated samples. For the

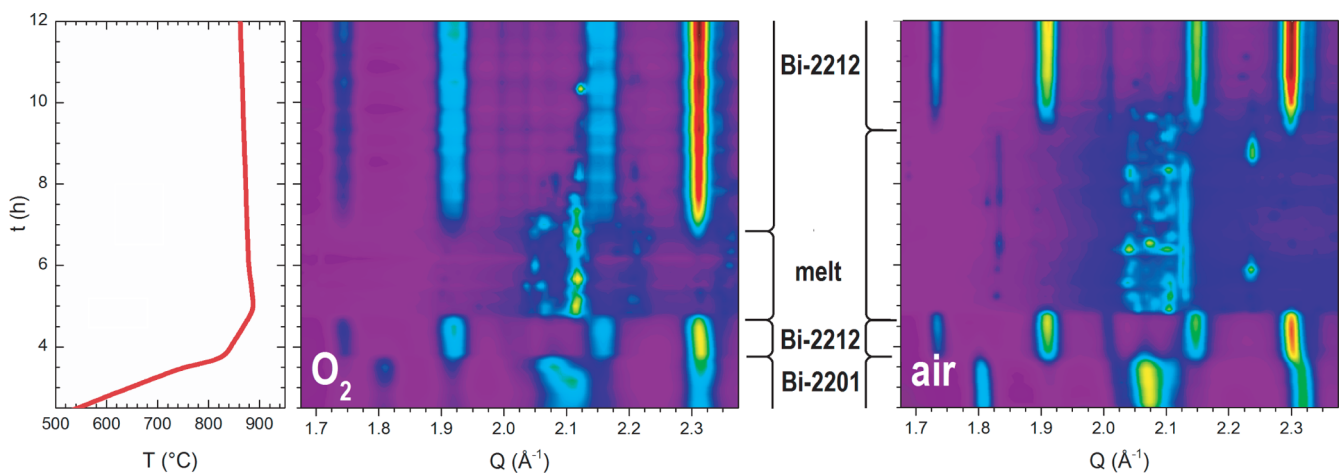


FIG. 7. Phase evolution in the multifilamentary wires during the first 12 hours of the thermal treatment in O₂ (on the left) and air (on the right); selected Q-range of XRD data.

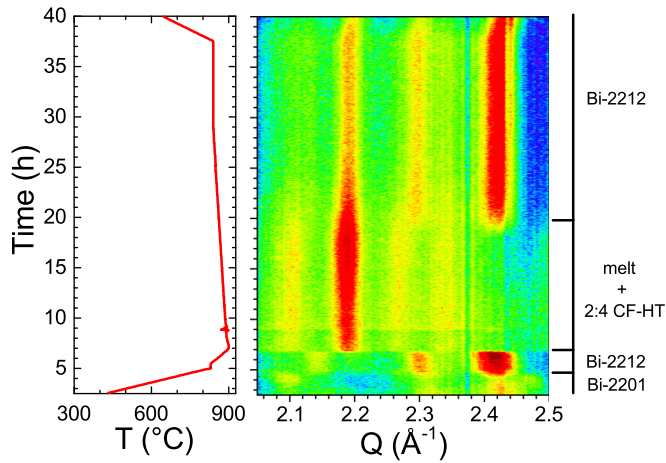


FIG. 8. Phase evolution in the multifilamentary wires (thermal treatment TT2 in O₂); selected Q-range of NPD data.

O₂-treated sample, the intensity rapidly increases and then almost saturates, indicating that the Bi-2212 phase undergoes at first a fast growth. Later the intensity of the 110 peak remains approximately constant with time, suggesting that the amount of Bi-2212 does not change significantly. In the air-treated sample, where the growth of the Bi-2212 phase is substantially delayed, the formation of the Bi-2212 phase grows as well rapidly before entering a different regime where the reaction leading to the formation of the Bi-2212 is still taking place, although slowed down. On the basis of our data, it is not possible to ascertain if the reduced oxygen activity in the air-treated sample directly slows down the kinetic of formation

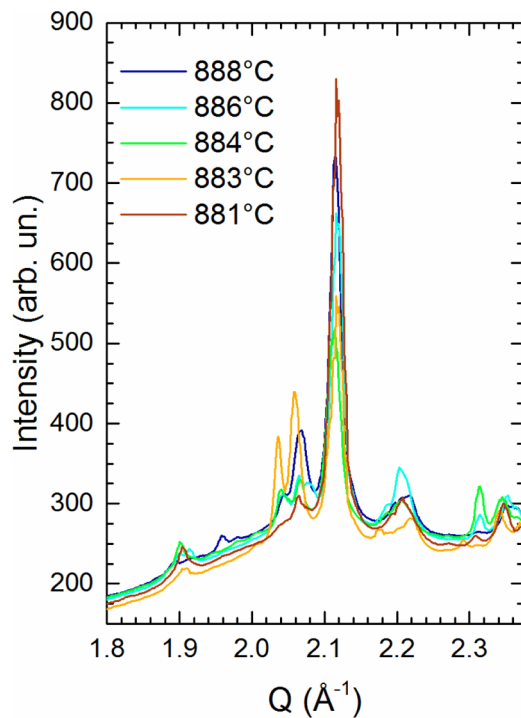


FIG. 9. Evolution of the phase relationship with time within the melted filaments (O₂ treated sample); XRPD diffraction patterns are collected every 10 min.

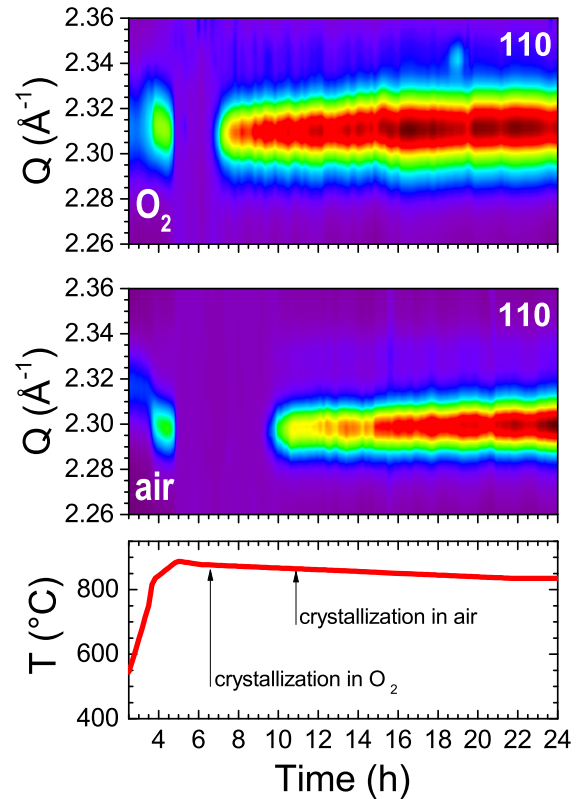


FIG. 10. Time dependence of the 110 diffraction line of the Bi-2212 phase during the thermal treatments in O₂ and air (XRPD data).

of Bi-2212 or else favours the formation of secondary phases, whose growth competes with that of Bi-2212.

Figure 12 shows the texturing evolution of the Bi-2212 phase after crystallization from the melt during the thermal treatments in O₂ and air obtained from the refined texture parameter. Remarkably, more than 95% of the sample treated under an O₂ atmosphere is textured along [110] as the phase

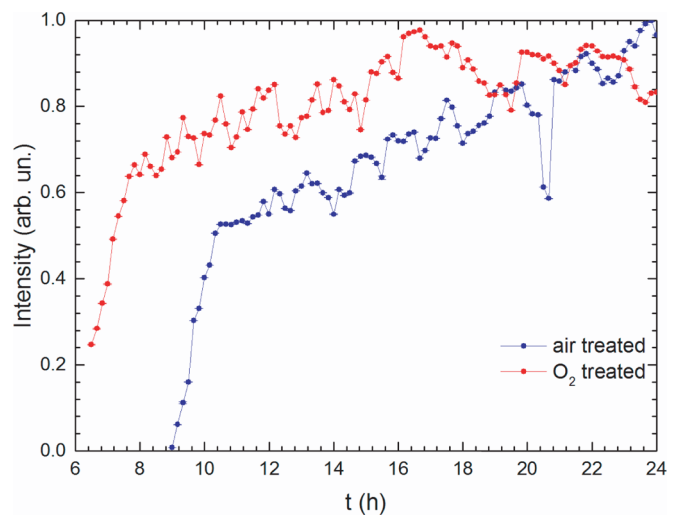


FIG. 11. Time evolution of the integrated intensity for the tetragonal 110 diffraction line after the crystallization of the Bi-2212 phase from the melt (normalized data).

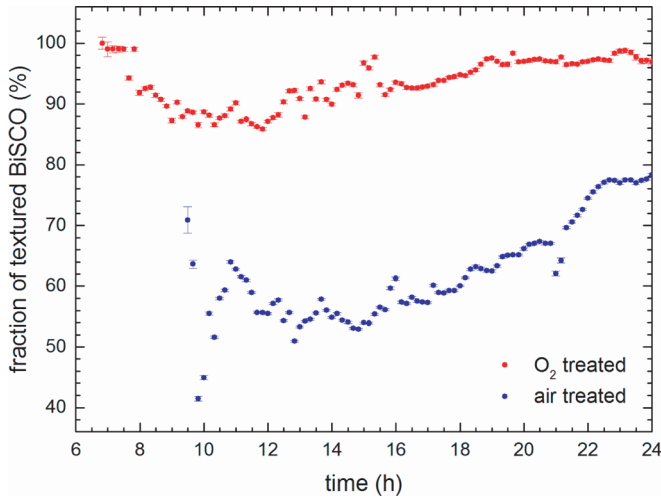


FIG. 12. Evolution of the fraction of textured Bi-2212 phase as function of time during the thermal treatments in O₂ and air.

appears early after the melting; the sample treated in air displays as well a notable texturing along the same direction, but the amount of oriented phase is significantly reduced. Noteworthy, the refinement of the preferred orientation parameters indicates that in all samples the Bi-2212 crystals are characterized by a prevailing platylike habit.

To deeply investigate the texture evolution, we directly studied the spatial distribution of the diffracted peak in the 2D acquired images (see Fig. 13). Indeed, due to the strong texturing, the angular distribution of the Bragg peaks is uneven and not equally distributed along Debye Scherrer rings (at constant Q) as expected for randomly oriented powders. Analyzing several Bragg peaks belonging to different $\{hkl\}$ families and assuming a cylindrical symmetry along the axis of the wire, it is possible to extract from the images the orientation distribution of the superconducting grains inside the filaments. The position of the peaks gives a biaxial orientation in agreement with the results of Kametani *et al.* [27] with the c axis laying in a plane normal to the RD (wire direction) and a less pronounced preferential orientation of the basal axes in the wire direction; analyzing the azimuthal angular dispersion of Friedel pairs a FWHM of about 15° and 30° can be estimated for the two directions, respectively.

We also analyzed the origin and the evolution of this texture during the thermal treatment of the wire. In Fig. 14, the intensity of the 008 (b) and 105 (c) peaks for the O₂ treated sample as a function of the azimuth angle (horizontal axis) and of the time (vertical axis) are reported. Following the evolution of these two peaks it is possible to evaluate the progression of the c -axis texture and of the basal plane, respectively. A small degree of texturing, with the platylike grains oriented along the rolling direction [Fig. 14(b)] (c axis in the normal directions) but no in-plane texture is present [Fig. 14(c)] at the beginning of the thermal treatment. This effect is due to the cold working process that forces the grain to align with their largest dimension in the deformation directions, in a similar way on what happens in the Bi-2223 tapes fabrication where this effect is then amplified by the flat rolling. The strong texture appears instead immediately when the Bi-2212

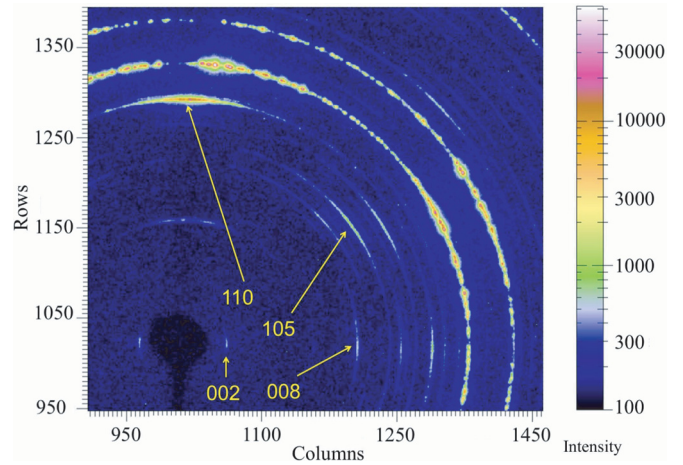


FIG. 13. Acquired diffraction image showing the distribution of the spot.

phase starts to crystallize after the “melt” and no further significant effects are observed during the rest of the thermal treatment.

A similar behavior is observed in samples prepared in air but some differences are present in the diffraction pattern, indicating a relatively more disordered structure with a more discrete distribution of the grain orientation (see Figs. 14 and 15). The orientation is here again determined at the nucleation and crystallization point. Different from the sample treated in O₂, it is, however, possible to observe some grains that during the first part of the cooling process rotate slightly (marked by arrows on Fig. 15(c), but the overall original orientation acquired at the nucleation is kept during the process.

E. Growth of the secondary Bi-2201 phase

In parallel with the crystallization and texturing of the Bi-2212 phase, also the growth of the Bi-2201 phase is observed following the melting step, as evidenced by the growth and

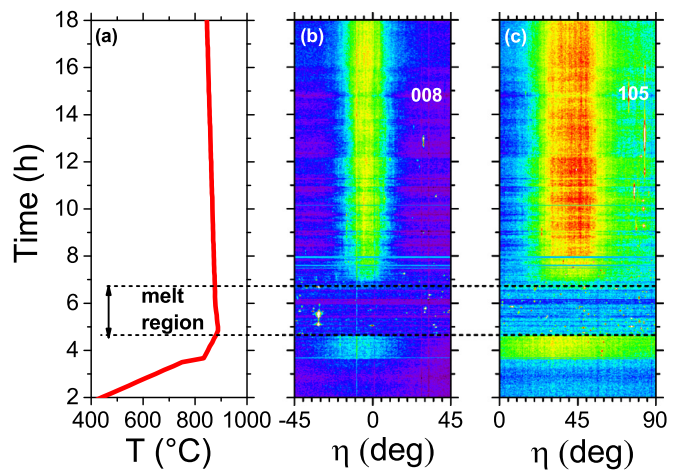


FIG. 14. Intensity of the 008 (b) and 105 (c) peaks as a function of the azimuth angle (horizontal axis) and of the time (vertical axis) during the thermal treatments in O₂ (a).

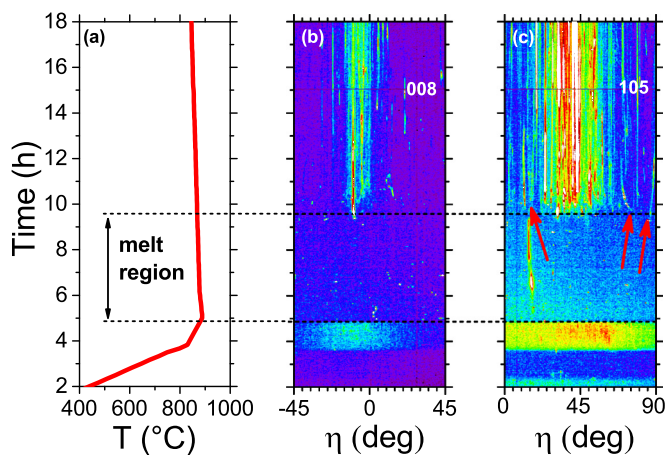


FIG. 15. Intensities of the 008 (b) and 105 (c) peaks as a function of the azimuth angle (horizontal axis) and of the time (vertical axis) during the thermal treatments in air (a).

evolution of the 151 peak with time (Fig. 16). Using the Rietveld method, the weight percentage of the Bi-2201 phase can be determined to $\sim 9.0(2.0)\%$ in the air-treated sample at the end of the thermal treatment, whereas in the O_2 -treated sample this percentage is notably suppressed, being only $6.4(1.0)\%$. It is important to notice that, in this case, the considered Bi-2201 phase percentage corresponds to the one coexisting as a secondary phase with the main Bi-2212, not to the percentage which is intragrown within it (see Sec. III B). Remarkably, the amount of both Bi-2212 and Bi-2201 phases increases with time during the plateau step in the air-treated sample, suggesting that the formation processes of these phases compete for the same reactants.

F. Analysis of the fully reacted samples

The synchrotron XRD data collected on the fully reacted samples has been fitted using the Rietveld method for estimat-

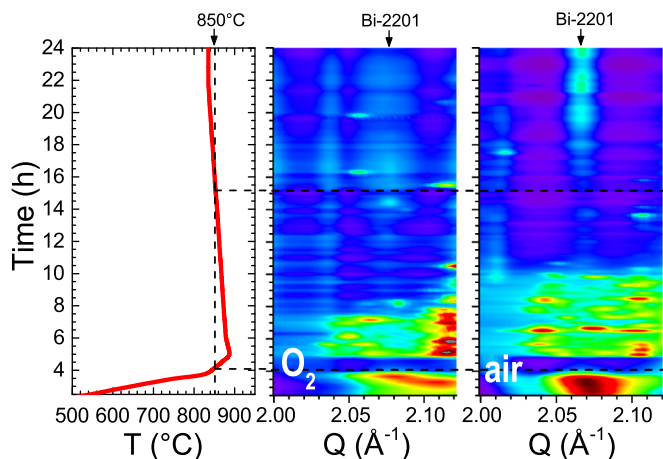


FIG. 16. Evolution of the highest intensity 151 diffraction line of the Bi-2201 phase in the O_2 and air-treated samples (XRPD data). After melting, the presence of this phase is hardly detectable in the O_2 treated sample; conversely, it is clearly observed in the air treated sample and its mass percentage increases with time.

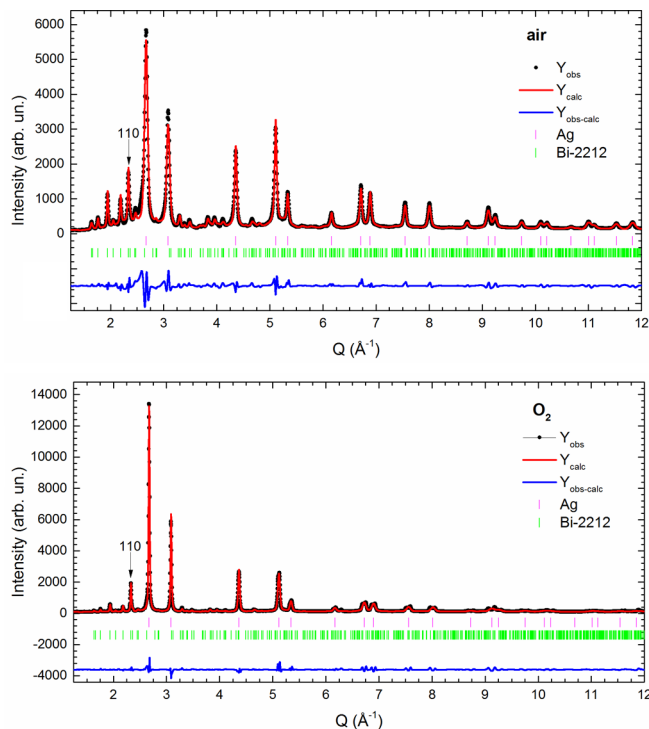


FIG. 17. Rietveld refinements obtained for the fully reacted samples (XRD data collected at room temperature); the 110 diffraction line of the Bi-2212 phase marking the texturing of the samples is arrowed; upper and lower vertical bars indicate Bragg reflections for Ag and Bi-2212, respectively.

ing the weight percentage of the phases. The obtained results are in good agreement with the afore-reported data, indicating a degree of texturing for Bi-2212 of 99% and 80% after the thermal treatments in O_2 and air, respectively (Fig. 17). Several medium-to high intensity peaks pertaining to the Bi-2212 phase can be recognized in the air-treated sample, although the 110 diffraction line (arrowed) exhibits the highest relative intensity, thus indicating a marked texturing. Differently, in the O_2 treated sample, only the 110 diffraction line is characterized by a high relative intensity, all the other peaks displaying weak-to-undetectable intensities, thus confirming the higher degree of texturing in this sample.

The structural data resulting from the fits are reported in Table II; remarkably, the amount of secondary Bi-2201 phase appears to increase with the decrease of the c axis of the Bi-2212 phase.

TABLE II. Cell parameters and weight percentage of $Bi_2Sr_2CuO_{6+x}$ and $Bi_2Sr_2Ca_1Cu_2O_{8+x}$ phases at the end of the thermal treatment TT1 in air and O_2 (fully reacted samples; XRD data collected at room temperature).

	Air	O_2
a (Å)	3.8033(1)	3.8146(1)
c (Å)	30.6504(6)	30.7866(7)
Bi-2212 (wt%)	91.22(4.46)	95.43(5.9)
Bi-2201 (wt%)	8.78(2.0)	4.47(2.53)

TABLE III. Structural data of Bi-2212 and weight percentage of secondary Bi-2201 phase at different steps during the O₂ thermal treatment TT2.

		24 h/835 °C	29 h/835 °C	36 h/295 °C
Bi-2212	a (Å)	3.9301(1)	3.9297(1)	3.8994(1)
	c (Å)	31.635(1)	31.632(1)	31.4092(6)
Bi-2201 (wt%)		3.0(9)	3.2(4)	5.3(5)

Data collected on the O₂ treated sample after 24 h (835 °C), 29 h (835 °C), and 36 h (295 °C) during the thermal treatment TT2 are compared in Table III. Seemingly, the prolonged annealing at 835 °C produces no significant change of the structural properties of Bi-2212 and even the amount of secondary Bi-2201 remains constant. This conclusion must, however, be taken with caution since it is based on diffraction data of relatively low quality, being influenced by the scattering and absorption of the Ag sheet.

G. Microstructural analysis of the silver sheath

The different evolution of the phase assemblages and texturing in the multifilamentary wires treated under air and O₂ can be definitely ascribed to the different thermodynamic activity of oxygen within the samples. This phenomenon can be directly probed by the microstructural analysis of the Ag sheath, undergoing microstructural changes during the thermal treatments. Generally speaking, oxygen diffusion initially occurs along the grain boundaries, but as the temperature increases intragrain interstitial diffusion can be activated and the incorporation of O atoms in the Ag structure consequently induces lattice strains [29]. In particular, oxygen diffusion determines the anisotropic displacement of Ag atoms and the formation of structural defects. As a result, the resulting structural strains selectively broadens the diffraction lines, as evidenced in Fig. 18, where the Williamson-Hall plots obtained

from the two samples at the beginning (~70 °C) and at the end (~888 °C) of the heating step are superposed. Data collected from the air-treated samples display a decrease of the strain along all of the crystallographic directions, indicating that the lattice strains produced during the cold working of the wires are eliminated by the thermal treatment. Conversely, in the O₂ treated sample, a notable increase of the lattice strain develops along all the crystallographic direction, thus demonstrating the incorporation of O atoms in the Ag structure; that is, an effective diffusion of oxygen throughout the silver sheath. In particular, the microstructural properties observed for this sample are consistent with the results reported by Nagy *et al.* [29]. These authors stated that oxygen diffusion takes place along [220], thus producing strain broadening of the 220 diffraction line, as well as a similar broadening for the 111 and 311 diffraction lines, whose zone axis at the intersection of the corresponding planes is the same [220]; conversely, the 200 diffraction line exhibits a different behavior. This phenomenology can be exactly observed by comparing the Williamson-Hall plots of the O₂-treated sample. Based on these results, it can be concluded that in the air-treated sample, oxygen mainly diffuses along grain boundaries and bulk diffusion is essentially hindered; conversely, the selective lattice strain observed in the O₂ -treated sample proves the activation of the bulk diffusion, determining a larger thermodynamic activity of the oxygen within the filaments.

IV. DISCUSSION

The aim of the present paper is to give a contribution to the understanding of the processes actually occurring during the typical heat treatment in the Bi-2212 wire fabrication process. For the first time, *in situ* diffraction data have been collected giving insights into the phase assemblage and microstructural evolution inside a wire having been subjected to exactly the same conditions in which the wire is normally processed for application purposes. The results can thus have a direct repercussion on the production technology of such superconductors, improving their preparation. Furthermore, the observations reported here can partly clarify aspects and concerns left unsolved in previous works [14–16] regarding the phase formation, the evolution of the texture, the role of the oxygen on the transport properties, and the evolution of the secondary phase Bi-2201. All the analysis was performed on our laboratory-made wires; however, it is worth to underline that the obtained results are in full agreement with those observed on state-of-the-art Bi-2212 wires. Looking at the evolution of the phases in Fig. 8, we can observe that the Bi-2201 phase starts to grow well below the melting temperature. On the other hand, it is interesting to observe that this phase then decomposes again, forming novel Bi-2212 phase at 850 °C in both cases, air and O₂. If we look at what happens after the melting, during the slow cooling in which the recrystallization occurs (Fig. 15), new Bi-2201 phase appears again at about 850 °C, but in this case, its amount is determined by oxygen activity: in air it is about 9%wt while in pure O₂ it decreases to about 5%wt (Table II). It is as well interesting to notice that this amount is reached for both samples already after a few hours at the plateau at 836 °C, and remains substantially unchanged

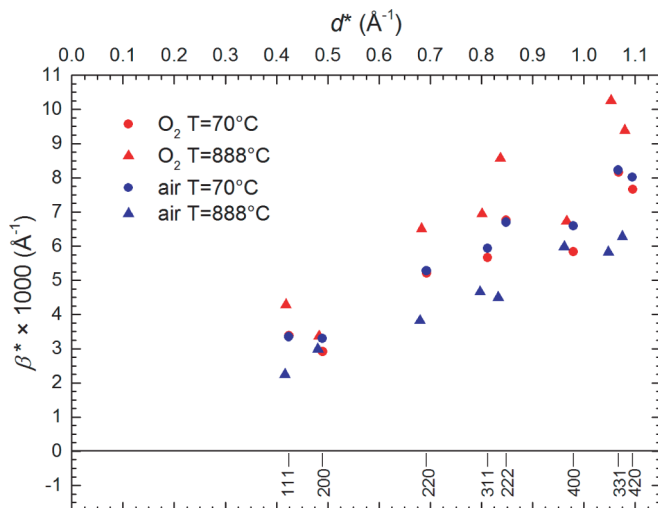


FIG. 18. Superposition of the Williamson-Hall plots obtained from the two samples at the beginning (~70 °C) and at the end (~888 °C) of the heating step; the vertical bars in the lower field indicate the positions of the indexed Bragg peaks.

in the fully reacted samples whose heat treatment includes a plateau at 836 °C for 48 h (Tables II and III).

It is well known that Bi-2201 grains, whose superconducting properties are very poor, represent an obstacle for the supercurrent flowing through Bi-2212 grains. From these results, we get a strong indication about a possible optimization of the parameters of the “standard” PMP aiming at the reduction of secondary phases and thereby at a J_c enhancement in conductors used in practice. A further comment has to be made about the Bi-2201 intragrowth layers. Naderi *et al.* [14] reports on the role of such intragrowths that, when their size is comparable with the coherent length of Bi-2212, can actually act as pinning centres, enhancing the transport properties at high field. We found that their density is approximately estimated as 6.5% in the O₂ sample, and almost negligible in the air sample. However, given the difficulty in making such a calculation in our experiment, we leave open the issue, pushing it back to a more proper and precise investigation.

The analysis of the texture evolution showed that the deformation process is able to induce, similar to the situation in the manufacturing process of Bi-2223 tapes, a preferential orientation of the *c* axis normal to the RD while no in plane orientation is present after the cold working process or in the first part of the thermal treatment, where the Bi-2212 phase partially recrystallizes. During the “melting,” obviously no Bi-2212 crystalline phase is detected, but simpler oxides are observed. The diffraction pattern of these phases does not correspond to a powder pattern with circular Debye Scherrer rings circles but appears as bright spots reflecting the formation of a few but large crystal grains. The spots are randomly distributed in the azimuthal direction, indicating that no preferential orientation is kept in this stage of the process.

Lowering the temperature, the Bi-2212 phase starts to crystallize (at different temperatures in O₂ atmosphere or air as previously discussed) and nucleates directly with a strong biaxial texture. In particular, the *c* axis of the Bi-2212 grains is narrowly distributed (FWHM 15) around the normal to the wire plane. A measurement performed on a fully reacted wire, without the furnace but mounted on a Φ stage, allowing rotating the sample around the wire axes, confirmed the cylindrical symmetry by showing no significant dependence of the pattern on the Φ angle. A smaller, but significant orientation (FWHM 30) is observed also for the distribution of the rotation of the grain around their *c* axis. The observed texture and its values are fully in agreement with the results of Kametani *et al.* [27] but, in addition to this work, we were able to observe that this texture originates from the nucleation of the Bi-2212 phase after the melt and does not depend on any texture previously induced in the powders. The successive steps in the thermal treatment

(slow cooling and plateau) affect the grain growth and the crystalline order of the phase but no effects are observed on the evolution of the texture for the sample treated in O₂. The sample reacted in air shows basically the same behavior. Its diffraction patterns reveals, however, a certain texture evolution during the plateau step and a number of grains showing different orientations are detected. In some cases, a tendency for these grains to align along the “main” orientation in the course of the thermal treatment is observed. In general, the degree of the final texture in the air-treated samples is lower than in O₂-treated ones, indicating that the oxygen activity plays a primary role.

V. CONCLUSION

In summary, we have presented an in-depth *in situ* analysis of the phase and its microstructure evolution in our laboratory-made Bi-2212 wires taking place during the heat treatment usually applied in the fabrication process. The results in terms of secondary phase detection and grain texture are not only in full agreement with what is reported for state-of-the-art wires, but also add important insights for a further optimization of the process itself. It is now clear when and at which temperature the Bi-2201 phase forms and, consequently, how to avoid it. As already observed before, the Bi-2212 phase shows an in-plane and an out-of-plane texturing but the here presented results reveal as well that the texture originates from the nucleation of the Bi-2212 grains and does not evolve during the successive steps of the treatment. The role of the oxygen activity has been better clarified with the demonstration that this parameter rules the Bi-2212 texturing. These findings are of great importance for reducing the amount of secondary phases and improving the degree of texture, the two key parameters for obtaining high J_c values.

These results should furthermore promote the development of other HTS materials as isotropic wires through a similar process.

ACKNOWLEDGMENTS

The authors acknowledge Dr. V Diadkin for his kind support and experimental assistance during the data collection at the ID11 beamline of ESRF Proposal No. MA-3116). Part of this work has been performed in collaboration with A. Ballarino and S. Hopkins from CERN within the Addendum FCC-GOV-CC-0086 of the Memorandum of Understanding FCC-GOV-CC-0004 for the FCC study. Finally, this work has been carried out also within the framework of the EUROfusion Consortium and has received funding from the Euratom Research and Training Programme 2014–2018 under Grant Agreement No. 633053. The views and opinions expressed herein do not necessarily reflect those of the European Commission.

-
- [1] J. Bascunan, S. Hahn, Y. Kim, J. Song, and Y. Iwasa, *IEEE Trans. Appl. Supercond.* **24**, 4300904 (2014).
 - [2] L. Bottura, G. de Rijk, L. Rossi, and E. Todesco, *IEEE Trans. Appl. Supercond.* **22**, 4002008 (2012).
 - [3] D. Larbalestier, A. Gurevich, D. M. Feldmann, and A. Polyaniskii, *Nature* **414**, 368 (2001).
 - [4] A. Malagoli, F. Kametani, J. Jiang, U. P. Trociewitz, E. E. Hellstrom, and D. C. Larbalestier, *Supercond. Sci. Technol.* **24**, 075016 (2011).
 - [5] F. Kametani, T. Shen, J. Jiang, C. Scheuerlein, A. Malagoli, M. Di Michiel, Y. Huang, H. Miao, J. A. Parrell, E. E. Hellstrom, and D. C. Larbalestier, *Supercond. Sci. Technol.* **24**, 075009 (2011).

- [6] C. Scheuerlein, M. Di Michiel, M. Scheel, J. Jiang, F. Kametani, A. Malagoli, E. E. Hellstrom, and D. C. Larbalestier, *Supercond. Sci. Technol.* **24**, 115004 (2011).
- [7] A. Malagoli, P. J. Lee, A. K. Ghosh, C. Scheuerlein, M. Di Michiel, J. Jiang, U. P. Trociewitz, E. E. Hellstrom, and D. C. Larbalestier, *Supercond. Sci. Technol.* **26**, 055018 (2013).
- [8] D. C. Larbalestier, J. Jiang, U. P. Trociewitz, F. Kametani, C. Scheuerlein, M. Dalban-Canassy, M. Matras, P. Chen, N. C. Craig, P. J. Lee, and E. E. Hellstrom, *Nat. Mater.* **13**, 375 (2014).
- [9] A. Leveratto, V. Braccini, D. Contarino, C. Ferdeghini, and A. Malagoli, *Supercond. Sci. Technol.* **29**, 045005 (2016).
- [10] A. Malagoli, V. Braccini, M. Vignolo, X. Chaud, and M. Putti, *Supercond. Sci. Technol.* **27**, 055022 (2014).
- [11] A. Malagoli, C. Bernini, V. Braccini, G. Romano, M. Putti, X. Chaud, and F. Debray, *Supercond. Sci. Technol.* **26**, 045004 (2013).
- [12] T. Shen, J. Jiang, F. Kametani, U. P. Trociewitz, D. C. Larbalestier, J. Schwartz, and E. E. Hellstrom, *Supercond. Sci. Technol.* **23**, 025009 (2010).
- [13] W. Zhang and E. E. Hellstrom, *Supercond. Sci. Technol.* **8**, 430 (1995).
- [14] G. Naderi and J. Schwartz, *Appl. Phys. Lett.* **104**, 152602 (2014).
- [15] C. Scheuerlein, J. Andrieux, M. Rikel, J. Kadar, C. Doerrer, M. Di Michiel, A. Ballarino, L. Bottura, J. Jiang, F. Kametani, E. Hellstrom, and D. Larbalestier, *IEEE Trans. Appl. Supercond.* **26**, 6400304 (2016).
- [16] I. Pallecchi, A. Leveratto, V. Braccini, V. Zunino, and A. Malagoli, *Supercond. Sci. Technol.* **30**, 095005 (2017).
- [17] R. Flukiger, Y. Huang, F. Marti, M. Dhalle, E. Giannini, R. Passerini, E. Bellingeri, G. Grasso, and J.-C. Grivel, *IEEE Trans. Appl. Supercond.* **9**, 2430 (1999).
- [18] E. Giannini, E. Bellingeri, R. Passerini, and R. Flükiger, *Physica C (Amsterdam)* **315**, 185 (1999).
- [19] J. Rodríguez-Carvajal, *Physica B (Amsterdam)* **192**, 55 (1993).
- [20] J. I. Langford, D. Louër, E. J. Sonneveld, and J. W. Visser, *Powder Diffr.* **1**, 211 (1986).
- [21] R. A. Young, ed., *The Rietveld Method*, International Union of Crystallography Monographs on Crystallography No. 5 (International Union of Crystallography, Oxford University Press, Chester, England, 1993).
- [22] J. B. Torrance, Y. Tokura, S. J. LaPlaca, T. C. Huang, R. J. Savoy, and A. I. Nazzal, *Solid State Commun.* **66**, 703 (1988).
- [23] P. Bordet, J. Capponi, C. Chaillout, J. Chenavas, A. Hewat, E. Hewat, J. Hodeau, M. Marezio, J. Tholence, and D. Tranqui, *Physica C (Amsterdam)* **153-155**, 623 (1988).
- [24] M. O. Rikel and E. E. Hellstrom, *Physica C (Amsterdam)* **357-360**, 1081 (2001).
- [25] C. C. Luhrs, E. Molins, G. Van Tendeloo, D. Beltrán-Porter, and A. Fuertes, *Chem. Mater.* **10**, 1875 (1998).
- [26] J. Kadar, C. Scheuerlein, M. O. Rikel, M. Di Michiel, and Y. Huang, *Supercond. Sci. Technol.* **29**, 105009 (2016).
- [27] F. Kametani, J. Jiang, M. Matras, D. Abraimov, E. E. Hellstrom, and D. C. Larbalestier, *Sci. Rep.* **5**, 8285 (2015).
- [28] A. Dellicour, B. Vertruyen, M. O. Rikel, L. Lutterotti, A. Pautrat, B. Ouladdiaf, and D. Chateigner, *Materials* **10**, 534 (2017).
- [29] A. J. Nagy, G. Mestl, D. Herein, G. Weinberg, E. Kitzelmann, and R. Schlögl, *J. Catal.* **182**, 417 (1999).